NANO LETTERS
Letter
Cite This: Nano Lett. 2018, 18, 1993−2000
pubs.acs.org/NanoLett

Three-Dimensional Integrated X-ray Diffraction Imaging of a Native Strain in Multi-Layered WSe_2

Mathew J. Cherukara,*[,†,#] Daniel S. Schulmann,[§,#] Kiran Sasikumar,[‡,#] Andrew J. Arnold,[∥] Henry Chan,[‡] Sridhar Sadasivam,[‡] Wonsuk Cha,[†] Jorg Maser,[†] Saptarshi Das,[⊥] Subramanian K.R.S. Sankaranarayanan,*[,‡] and Ross J. Harder*[,†]

[†]Advanced Photon Source and [‡]Center for Nanoscale Materials, Argonne National Laboratory, Argonne, Illinois 60439, United States
[§]Materials Science and Engineering, [∥]Electrical Engineering, and [⊥]Engineering Science and Mechanics, Pennsylvania State University, University Park, Pennsylvania 16802, United States

Supporting Information

ABSTRACT: Emerging two-dimensional (2-D) materials such as transition-metal dichalcogenides show great promise as viable alternatives for semiconductor and optoelectronic devices that progress beyond silicon. Performance variability, reliability, and stochasticity in the measured transport properties represent some of the major challenges in such devices. Native strain arising from interfacial effects due to the presence of a substrate is believed to be a major contributing factor. A full three-dimensional (3-D) mapping of such native nanoscopic strain over micron length scales is highly desirable for gaining a fundamental understanding of interfacial effects but has largely remained elusive. Here, we employ coherent X-ray diffraction imaging to directly image and visualize in 3-D the native strain along the (002) direction in a typical multilayered (∼100−350 layers) 2-D dichalcogenide material (WSe_2) on silicon substrate. We observe significant localized strains of ∼0.2% along the out-of-plane direction. Experimentally informed continuum models built from X-ray reconstructions trace the origin of these strains to localized nonuniform contact with the substrate (accentuated by nanometer scale asperities, i.e., surface roughness or contaminants); the mechanically exfoliated stresses and strains are localized to the contact region with the maximum strain near surface asperities being more or less independent of the number of layers. Machine-learned multimillion atomistic models show that the strain effects gain in prominence as we approach a few- to single-monolayer limit. First-principles calculations show a significant band gap shift of up to 125 meV per percent of strain. Finally, we measure the performance of multiple WSe_2 transistors fabricated on the same flake; a significant variability in threshold voltage and the "off" current setting is observed among the various devices, which is attributed in part to substrate-induced localized strain. Our integrated approach has broad implications for the direct imaging and quantification of interfacial effects in devices based on layered materials or heterostructures.

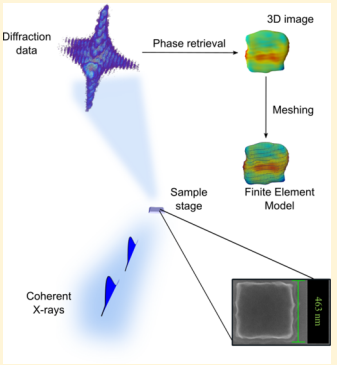

KEYWORDS: *Coherent X-ray imaging, 3-D strain mapping, multiscale modeling, chalcogenide layered semiconductors, WSe_2*

Two-dimensional transition metal dichalcogenides (TMDCs) have received a great deal of attention in the past decade owing to their exquisite physical and chemical properties that deviate significantly from their bulk counterparts. These properties have been exploited in a wide range of applications, including electrochemical storage involving lithium and sodium ion batteries, photocatalytic conversion, biosensors, and, most prominently, semiconductor and optoelectronics that progress beyond silicon.[1] In most of these applications, it is quite common for the TMDC to be supported on a substrate, embedded into other rigid structures, or form van der Waal heterostructures with other layered materials.[2] For example, recent efforts focus on the integration of TMDCs with Si-based substrates to enable logic component design. When supported on substrates, the TMDC experiences native strain arising from interfacial adhesion due to van der Waal interactions, which induces in-plane and out-of-plane structural deformations and excess charges.[3] Such subtle changes not only impact the properties (electronic and optical to name a few) of TMDCs but also are thought of as one of the major contributing factors to the reliability and variability in the performance of TMDC-based next-generation devices.

As bulk structures approach the few-layer or monolayer limit, it is well-known that the mechanical properties, degree of orbital interactions and electronic band dispersion of the crystal structure become highly sensitive to the applied strain and their distribution.[4−6] There are several different ways in which such native strain can develop in 2-D TMDC materials. TMDC layers experience varying degree of strain during their preparation (exfoliation or growth via CVD), the transfer

Received: December 27, 2017
Revised: January 26, 2018
Published: February 16, 2018

DOI: 10.1021/acs.nanolett.7b05441
Nano Lett. 2018, 18, 1993−2000

process and due to strong interfacial interactions in the postdeposition or post-transfer stage. Such residual or native strain at the interface can profoundly impact the electronic properties such as bandgap and band structure. For example, MoS_2 has been reported to show a band gap shift of up to 300 meV per 1% strain.[7] Likewise, multilayered WSe_2 shows an indirect-to-direct bandgap transition under applied strain of up to 2%.[8] Strain engineering in TMDCs is particularly interesting in the context of next generation ultralow power devices. In energy storage applications, it has been recently shown that a subtle MoS_2 strain of ∼0.1%, due to lattice mismatch between the carbon and MoS_2 layers, facilitated lithium ion intercalation as a result of an energy-efficient cation-exchange transformation.[9] Similarly, strained MoS_2/graphene heterostructures with increased interlayer spacing facilitate diffusion of intercalating ions and help to accommodate the volume changes during cycling.[10]

Direct imaging and visualization of strain in 2-D materials is thus highly desirable but has largely remained elusive. Most of the existing experimental characterization techniques rely on spectroscopy to infer the strain distribution in 2-D materials. As an example, Raman 2D modes have been recently used to measure strain levels in stretched graphene and TMDC monolayers.[11] Microscopy techniques such as high-resolution transmission electron microscopy (HRTEM) are commonly adopted for direct imaging of the atomic structure of the 2-D flakes. Likewise, a range of different scanning probe microscopy techniques from scanning tunneling microscopy (STM), atomic force microscopy (AFM), electrostatic force microscopy (EFM), Kelvin probe force microscopy (KPFM) to conductive atomic force microscopy (C-AFM), and photoconductive atomic force microscopy (PC-AFM), to name a few, have been employed in various capacities in the past for morphological and functional characterization of 2-D materials. While such spectroscopic and microscopy techniques are powerful and can be sensitive and accurate, they are most useful in assessing localized strains, especially near the surface. A full three-dimensional mapping of the nanometer-scale strain distribution over sizes up to micron length scales is most desirable to understand, control, and engineer strain in 2-D TMDC multilayered materials.

In this Letter, we introduce an integrated imaging approach in which we employ coherent X-ray diffraction imaging (CXDI), an emerging X-ray characterization technique in combination with continuum and atomistic scale modeling to directly image a native strain in three dimensions in a representative 2-D TMDC WSe_2. CXDI is a technique in which 3-D electron density and strains fields in a sample are obtained from scattered coherent X-rays in the far-field.[12] In contrast to electron beams, which are limited to sample thicknesses of ∼100 nm, CXDI provides full 3-D, local structural and strain information with ∼10 nm resolution in structures ranging from nanoparticles[13−15] to foams[16] to biological samples.[12,17] Finite element models have previously been used in conjunction with CXDI to aid the interpretation of CXDI data in which the retrieval of the real-space image was challenging[18,19] and to provide a physical interpretation of the observed deformation fields.[20] Through our CXDI measurements, we observe significant localized substrate induced native strains measured along the (002) crystallographic direction (averaging ∼0.2% with a maximum of ∼1.0%) close to the interface. To understand their origin, we subsequently input the reconstructed image into a continuum model to simulate the effect of localized nonuniform contact (typical of nanoscale surface roughness) on the native strain in multilayered (∼200 layers) 2-D WSe_2. Our results suggest that native strains are unlikely to have significant effects on the transport properties of multilayered TMDC's and can gain in prominence with reduction in the number of WSe_2 layers. To gain atomistic details into the strain distribution as we approach the few-layer to monolayer limit, we develop a machine learnt model of WSe_2 and perform multimillion atom simulations on a large-scale computing cluster to study the effect of localized loading on native strain in multilayered (∼50) to few-layer (∼10) WSe_2. Finally, we explore the potential effect of the measured residual strains on variability in such multilayered WSe_2-based devices.

Figure 1 shows a schematic of the experimental setup for CXDI performed at beamline 34-IDC at the Advanced Photon

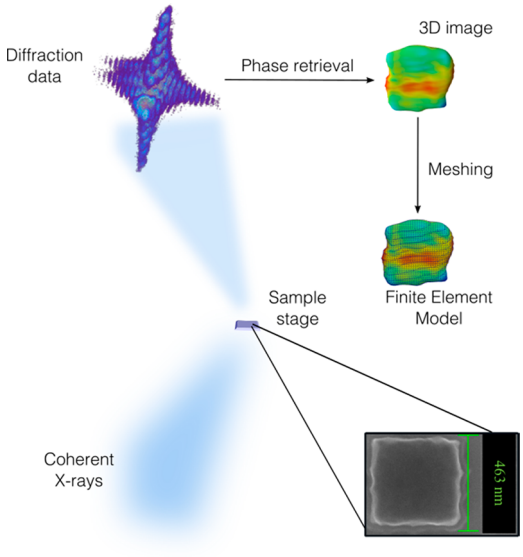

Figure 1. Coherent X-ray diffraction imaging. Coherent X-ray pulses generated from the synchrotron ring are used to image mechanically exfoliated WSe_2 nanoparticles (SEM image shown). The diffracted X-ray pulses are recorded by an ASI Timepix detector. The crystal structure recovered from the diffraction data was imported into the continuum model.

Source (APS). WSe_2 nanoparticles prepared through mechanical exfoliation and subsequent etching were placed on a sample stage at the center of a diffractometer (see the Methods section for details). The photon energy of the X-rays pulses was set to 9.0 keV using a Si (111) monochromator. Diffracted X-ray pulses from the sample were collected by an ASI Timepix detector in the (002) Bragg geometry.[21] By employing iterative-phase retrieval algorithms,[22,23] both the complex electron density $\rho(r)$ and the phase information $\phi(r)$ are recovered.[24,25] In turn, the phase information yields the atomic displacement field in the entire crystal volume through the relation $\phi(r) = \vec{Q}\cdot\vec{u}(r)$, where $\vec{u}(r)$ is the atomic displacement and $\vec{Q}$ is the scattering vector.[26] Additional details are described in the Methods section.

Figure 2 shows projected displacements along the (002) direction of two representative WSe_2 nanoparticles that were obtained following exfoliation and etching as described in the Methods section. Figure 2A,D shows isosurfaces of the electron density in the nanoparticles colored by the lattice displacement

DOI: 10.1021/acs.nanolett.7b05441
Nano Lett. 2018, 18, 1993−2000

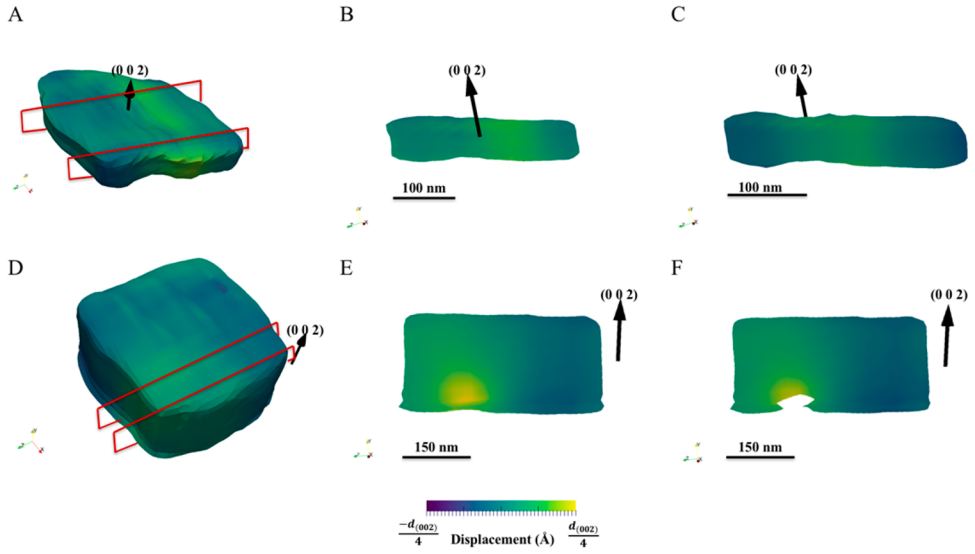

Figure 2. CXDI imaged lattice displacements along the (002) direction for two WSe_2 nanoparticles. Panels B and C show slices along the breadth of the crystal along the planes indicated in panel A, while panels E and F show slices long the planes indicated in panel D. Significant compressive strain is seen along the base of the second crystal.

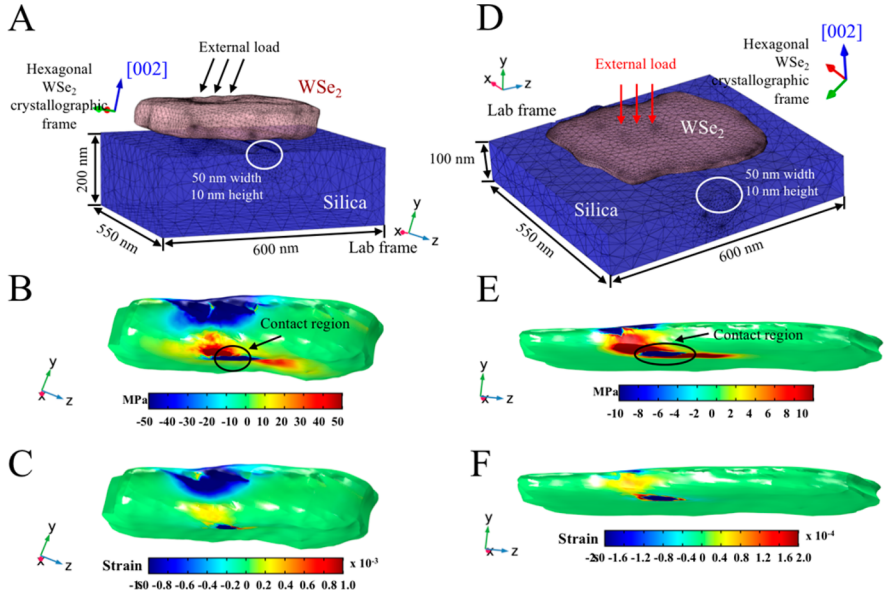

Figure 3. (A) Coherent X-ray diffraction imaging (CXDI) reconstructed WSe_2 structure (thickness is ∼80 nm) is imported into an FEM model in which the hexagonal WSe_2 structure is compressed against a silica substrate with a model cylindrical asperity (50 nm width and 10 nm height). (B) The first principal invariant of stresses on the WSe_2 sample is shown here. The color map is saturated for better visualization. Blue regions are in compression, and the red regions are in tension. The maximum compressive stress near the contact region is seen to be 1.70 GPa despite low external loads. (C) The observed strains near the contact region is comparable to experiments. The maximum compressive strain in the sample is 0.99% but confined to very small regions. (D) The CDI reconstruction is scaled down along (002) by a factor of 4 to mimic typically exfoliated flakes used for device measurements (<20 nm thickness). The scaled reconstruction is imported into an FEM model in which the hexagonal WSe_2 structure is compressed against a silica substrate with a model cylindrical asperity that represents surface roughness. (E) The first principal invariant of stresses on the corresponding WSe_2 sample. The color map is saturated for better visualization. Blue regions are in compression and red regions are in tension. (F) The local strains in the WSe_2 flake.

projected along the (002), while panels B and C and panels E and F show the displacement field along slices marked out in Figure 2A,D. The first nanoparticle (Figure 2A−C) has a thickness of ∼60 nm (∼100 layers), while the second has a thickness of ∼200 nm (∼350 layers). This is in good agreement with the thicknesses estimated from the wavelength, detector distance and the fringe spacing for the first and second crystals (85 and 210 nm) (see Figure SM 6). Supplementary Figure SM 3 shows an alternative view that highlights volumes with the maximum displacement and strain. As can be inferred from the displacement and strain maps, crystal 2 in particular shows significant strain, especially near the base of the crystal, potentially due to the influence of asperities on the substrate surface (represented by black wedges in Figure SM3).

Mechanical exfoliation involves application of difficult-to-measure, nonuniform loading on the flakes while pressed against the substrate. It is reasonable to expect the flakes to have nonuniform and localized contact with the substrate under

DOI: 10.1021/acs.nanolett.7b05441
Nano Lett. 2018, 18, 1993−2000

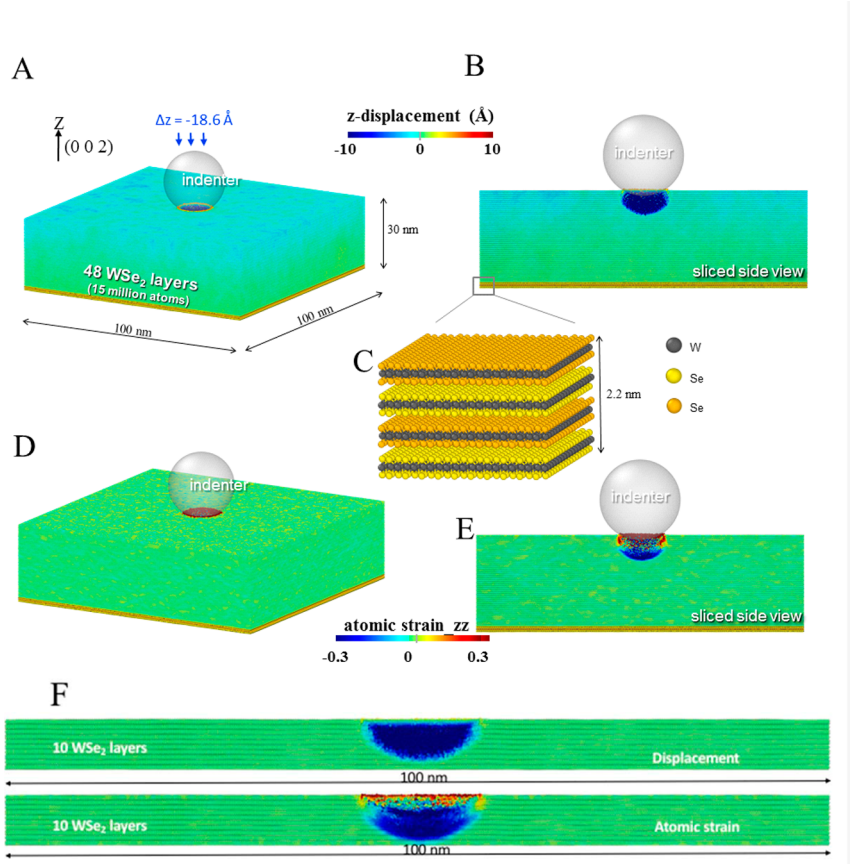

Figure 4. Mechanical deformation of a multilayer WSe_2 structure performed in an all-atom MD simulation. (A, D) 3D overview and (B, E) sliced side view of a multilayered (48 layers) WSe_2 structure at an indentation of 1.86 nm. Atoms that are not spatially fixed during the simulation are colored by their z-displacement and zz component of the atomic strain tensor, respectively. (C) Schematic of the system showing the arrangement W and Se atoms and the colors indicate their type assignment. (F) Sliced side view of few-layer (10-layer) WSe2 structure showing both the displacement and atomic strain at an indentation of 1.86 nm.

such conditions. Any surface roughness only accentuates this nonuniformity. Such nonuniform loading on individual flakes during mechanical exfoliation may result in significant variability in strain distribution across samples. In this work, we seek to demonstrate how localized contact with the substrate can result in permanent plastic deformation in segments of the flake. To perform a comparative simulation that directly complements the observed experimental results, the X-ray imaged crystal structure was used as an input to a mechanics simulation, at both continuum and atomistic scales. In the continuum model, the imported crystal surface is suitably meshed with tetrahedral units of sizes between 1 and 50 nm (see the finite element model (FEM) simulation in Figure 3). To mimic experimental conditions of mechanical exfoliation, a multiphysics simulation model including solid mechanics and explicit contact elements was built in COMSOL. The hexagonal WSe_2 structure is compressed against a silica substrate with a model cylindrical asperity (50 nm width and 10 nm height) that represents surface roughness. While we choose a large representative surface asperity in this work, it only serves as a way to induce localized contact with the substrate. In the Supporting Information, we present results for a perfectly smooth silica surface as well. We see that the exact size of the asperity does not affect our conclusions. The solid mechanics module along with suitably defined contact pairs between WSe_2 and silica surfaces are used to solve for the stationary stresses and strains. The bottom surface of silica is maintained as a fixed constraint. See the Methods section for additional details.

The material properties are defined with respect to the crystallographic frame (shown in Figure 3A,D). For a maximum (002) projected elastic displacement of the mesh nodes of 1.62 Å (similar magnitudes as the experimental reconstruction), the calculated contact force (which is equivalent to the external load applied during mechanical exfoliation) on a single WSe_2 flake is 2×10^{-7} N. Over a 1 cm × 1 cm scotch tape, with multiple flakes distributed with a density of 1 flake every 1.5 μm × 1.5 μm surface area; this translates to a total force of 9 N. This is within the range of typical forces that can be exerted by a human finger.[27] Figure 3B shows the first principal invariant of stresses on the WSe_2 sample. Despite the low external loads, the maximum compressive stress near the contact region is seen to be 1.70 GPa. The yield stress of WSe_2 for in-plane straining may be estimated from the stress−strain curves[28] to be ∼5.1 GPa. Stresses beyond the yield point will result in local plastic deformation in the sample, which remain as residual strains during device operation. For the 1.70 GPa maximum compressive stress case, the observed strains near the contact region (Figure 3C) are comparable to experiments, with a maximum compressive strain of 0.99% confined to very small regions of the sample making direct contact with the asperity surface. From the stress−strain curve of WSe2,[28] one may calculate that to obtain a 0.99% plastic strain the required compressive stress is 7.87 GPa (see the Supporting

DOI: 10.1021/acs.nanolett.7b05441
Nano Lett. 2018, 18, 1993−2000

Information). This is possible with a total force exerted during mechanical exfoliation over a 1 cm × 1 cm scotch tape of ~41 N.

To verify if the result holds for thinner WSe_2 flakes used in device measurements, we scale the coherent diffractive imaging (CDI) reconstruction down along (002) by a factor of 4 (Figure 3D–F). The new thickness mimics typical exfoliated flakes used for device measurements. The scaled reconstruction is, then, imported into the FEM model in which the WSe_2 flake is compressed against a silica substrate with a model asperity (Figure 3D). Here, we see that a 0.99% plastic strain will remain near the flake-substrate contact when the local stress is 7.87 GPa. This translates to a ~ 36 N force on a 1 cm × 1 cm scotch tape, with multiple flakes distributed with a density of 1 flake every 1.5 μm × 1.5 μm surface area. Furthermore, we see that the stress and strain fields near the asperity contact penetrates the entire thickness of the sample.

Furthermore, we also investigate the effects of external loading (both direction and magnitude) and the surface roughness of the substrate (see the Supporting Information for details). We observe that while these affect the stress distribution in the sample after mechanical exfoliation, the stresses and strains are localized to the contact region. These highly localized residual strains can contribute to variability in transport measurements of mechanically exfoliated multilayered TMDC devices and can gain in prominence with reduction in the number of WSe_2 layers (as the strained region represents a greater percentage volume of the sample).

Next, all-atom molecular dynamics (MD) simulations were performed to investigate the mechanical deformation of a multilayer WSe_2 structure and obtain atomistic scale descriptions of the same. The system consists of 48 WSe_2 layers (100 nm × 100 nm × 30 nm in size, total of 15 million atoms), which is periodic in the in-plane directions. The interactions between intralayer W and Se atoms are modeled using a bond-order potential based on the Tersoff formalism, while the interactions between WSe_2 layers are modeled via the Lennard–Jones potential by assigning different atom types to Se atoms in alternating layers (Figure 4C). The system was first equilibrated for ~0.3 ns under an isothermal–isobaric ensemble at T = 300 K and P = 1 bar, followed by mechanical deformation at a rate of 0.24 Å/ps using a spherical indenter with a radius of R = 12.5 nm. The bottom-most three WSe_2 layers were spatially fixed to prevent vertical shift of the system during the mechanical deformation. Displacement and strain maps of the system at an indentation of 1.86 nm roughly correspond to the results obtained from CDI experiments. The MD results show that the deformation is localized in the region directly below the indenter (representative of a nanoscale contaminant on the surface as a result of mechanical exfoliation), which is consistent with the CXDI results (Figure 4A–E). As the number of WSe_2 layers is reduced to ~10, we observe that the magnitude of deformation is similar but the strained region in the few-layer system now represents a greater percentage of the total volume. The results from the FEM and all-atom simulations suggest that the experimentally observed strain fields are indeed due to localized contact with the substrate. The consistency in the results from both MD and FEM, while seemingly intuitive, is far from trivial. This indicates that the continuum deformation model used in FEM and the resultant inferences we make are also applicable to few layer 2D materials at the atomic level. In the following section, we investigate whether the observed and simulated strain fields have an effect on the device performance and to what extent.

Figure 5A shows the false color SEM image of multiple (5) back-gated field effect transistors (FETs), each having the same

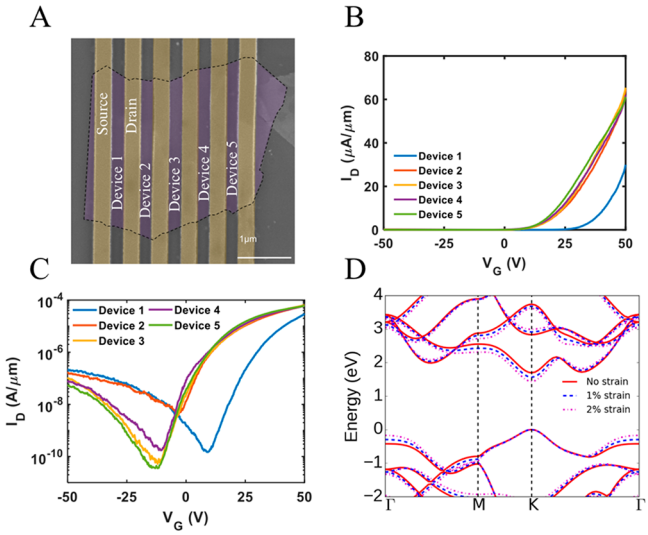

Figure 5. Mechanically exfoliated WSe_2 transistor characteristics. (A) SEM image of back gated WSe_2 transistor with a 100 nm thermal SiO_2 on p^{+2} Si substrate with Ni/Au contacts and 230 nm channel length. (B, C) Drain current (I_D) vs applied gate voltage (V_G) in linear scale and log scale with V_D = 1 V for 5 adjacent channels on the same flake showing significant variability in threshold voltage and the "off" current setting. (D) First-principles calculations of band structure of WSe_2 for varying in-plane strains.

channel length (L_{CH} = 230 nm), fabricated on a single WSe_2 flake. Electron beam lithography was used to pattern the contact regions followed by electron beam evaporation of the Ni/Au contacts. The linear-scale transfer characteristics are shown in Figure 5B with the log-scale measurements in Figure 5C. WSe_2 devices typically show ambipolar device characteristics, i.e., the presence of both electron and hole conduction with the asymmetry being determined by the relative position of the metal Fermi level with respect to the middle of the bandgap.[29] In our devices, the dominance of electron conduction suggests that the Ni Fermi level pins closer to the conduction band, which is consistent with earlier findings. From the device characteristics, it is apparent that Device 3 and Device 5 have relatively consistent characteristics with subthreshold slope (SS), threshold voltage (V_T), "off"-state current, and "on"-state current for both electron and hole branch varying by less than ~10% between these two devices. Such a small variation is generally attributed to randomness of charged impurities in the oxide, vacancies in WSe_2, presence of adsorbates at the interface, remote phonon scattering, etc.[30,31] Device 1 and Device 4 also have similar characteristics in terms of SS and "off" current; however, Device 1 has a significant positive threshold voltage shift and, hence, dramatically reduced "on" current in the electron branch and equally improved "on" current in the hole branch. Also note that the "off" current for the pair, Device 1 and Device 4, is slightly higher than for the pair of Device 3 and Device 5. Furthermore, Device 2 shows remarkably different characteristics with much higher "off" current and improved "on"-state hole current. These abrupt changes in threshold voltage and "off"-state current for devices on the same flake with same contact metal and same channel

DOI: 10.1021/acs.nanolett.7b05441
Nano Lett. 2018, 18, 1993–2000

dimensions cannot be attributed to aforementioned perturbations. However, a change in bandgap can give rise to different alignment of the metal Fermi level, which can significantly influence the threshold voltage as the Schottky barrier height gets modified. In addition, it is known that strain influences the bandgap by ~38 meV/GPa for WSe_2.[32] Indeed, our first-principles calculations shown in Figure 5D suggest a bandgap change of ~125 meV per percent of strain for WSe_2, which is consistent with previous reports.[33] This indicates that the large reduction in "off"-state current observed in these devices could be related to bandgap change, which can be introduced through local strain as reported here.

In summary, we have used coherent X-ray diffraction imaging to image in 3D the residual strain in exfoliated flakes of WSe_2. We observed significant strain near the base of one of the crystals as well as from simulations for both few-layer and thicker samples of WSe_2. Through the use of continuum and MD simulations, we trace the origin of the strain to localized contact with nanoscale asperities on the substrate. Finally, we studied the performance of multiple devices fabricated from the same exfoliated few-layer flake. We observed significant variation in the threshold voltage and "off"-state current in several of the fabricated devices. While the results presented here do not eliminate other sources of device variability, the presence of significant residual strain over extended volumes is a possible cause. To the best of our knowledge, this is the first reported 3D imaging of the strain within TMD materials, or layered materials in general. We expect that the characterization and simulation techniques presented here will prove valuable to the nondestructive testing and process optimization of fabricated devices.

Methods. *Sample Preparation.* WSe_2 bulk crystals were commercially purchased (2D Semiconductors Incorporation for the CXDI imaging and Nanosurf Incorporation for the transistors fabrication) and mechanically exfoliated onto a Si substrate with a 300 nm thermal oxide. The main challenge with CXDI of 2-D materials lies in the sample preparation. Hence, for the CXDI samples, with the aid of prepatterned metal fiducials on the substrate, flakes with lateral dimensions of at least 50 μm, and thicknesses greater than 50 nm were identified using an optical microscope and camera. A Raith EBPG5200 electron-beam lithography tool was then used to pattern ZEP520A photoresist for the subsequent etch step. A sulfur hexafluoride plasma based reactive ion etch was performed in a Plasma-Therm Versalock 700 to pattern the flakes defining 500 nm × 500 nm nanoparticles spaced at least 30 μm apart on each flake. A 10 μm × 10 μm nanoparticle with the same orientation as the smaller nanoparticles was patterned as a fiducial marker to the smaller flakes, which were the object of the study. The photoresist was not removed from the sample to prevent the nanoparticles from being released into the photoresist removal solution. After patterning, the nanoparticles were inspected by scanning electron microcopy.

CXDI Measurement. Coherent diffraction data was collected in the specular geometry with the detector and sample stage placed at the appropriate angles corresponding to the (002) Bragg peak. To acquire the 3D coherent pattern about the (002) Bragg peak, the sample stage was rotated through 1.2° in steps of 0.01° with an exposure time of 1 s. The detector was placed at a distance of 0.7 m for the first nanoparticle and at a distance of 1.0 m for the second nanoparticle, which was sufficient to over-sample the diffraction pattern in all dimensions. Subsequently, the real space intensity and phase were recovered through the guided approach of Chen et al.[34] The crystal dimensions were 300−500 nm in the longest dimension, well within the coherence lengths of $\xi_{horizontal}$ = 12 μm, $\xi_{vertical}$ = 300 μm, and $\xi_{longitudinal}$ = 0.65 μm.[24,35] A total of 4 generations of 10 individuals each were used in the guided reconstruction. At every generation, each individual was bred with the best individual (as defined by the sharpness metric) from the previous generation before being further refined through 620 iterations of hybrid input output plus error reduction.

Finite Element Model. The CDI reconstruction of the WSe_2 flake is imported into the finite element method (FEM) code, COMSOL, to characterize the local deformation upon mechanical exfoliation. In the multiphysics model including solid mechanics and explicit contact elements, the hexagonal WSe_2 structure is compressed against a model silica substrate with different surface asperities that represent the surface roughness. The nonlinear contact mechanics problem is solved iteratively by applying incrementally small displacements to the top surface of WSe_2, with contact forces, steady-state stresses, and strains obtained for each case. Such a displacement boundary condition (as opposed to applying a boundary force) is necessary to solve such contact mechanics problems due to stability issues of the finite element mesh. The material properties for WSe_2 and silica are defined with respect to the respective crystallographic orientations (see the Supporting Information for details).

Molecular dynamics. MD simulations of WSe_2 multilayer structures were performed using LAMMPS on the supercomputing resources at the Argonne Leadership Computing Facility. The interactions between intralayer W and Se atoms were modeled using a Tersoff potential, while the interlayer interactions were modeled using a Lennard−Jones potential. The initial structure of WSe_2 layers was relaxed via energy minimization and equilibrated at a time step of 0.5 fs in an isothermal−isobaric ensemble, with a thermostat and barostat relaxation time scale of 0.005 and 0.5 ps, respectively. Mechanical deformation of the WSe_2 structure was simulated in a canonical ensemble using a virtual spherical indenter. Throughout all simulations, periodic boundary conditions were applied to the in-plane (x- and y-) directions of the WSe_2 layers.

Density Functional Theory. The electronic band structure of monolayer WSe_2 is computed using density functional theory, as implemented in the Quantum Espresso package[36] with LDA norm-conserving pseudopotentials. A plane wave kinetic energy cutoff 80 Ry and a k-point grid of 12 × 12 × 1 are used in the calculations. The change in band structure due to tensile strains of 1% and 2% along both in-plane lattice vectors are shown in Figure 5D. The direct bandgap is found to reduce by 0.13 and 0.25 eV for 1% and 2% strains, respectively.

■ ASSOCIATED CONTENT

Supporting Information

The Supporting Information is available free of charge on the ACS Publications website at DOI: 10.1021/acs.nanolett.7b05441.

Additional details on the CDI-informed FEM model. Figures showing the effects of external loading and surface roughness, CDI-reconstructed structures, stress−strain curves, displacement fields and corresponding strain maps, slices of strain, mechanical deformation, and 3D coherent diffraction images. (PDF)

DOI: 10.1021/acs.nanolett.7b05441
Nano Lett. 2018, 18, 1993−2000

AUTHOR INFORMATION

Corresponding Authors

*E-mail: mcherukara@aps.anl.gov.
*E-mail: skrssank@anl.gov.
*E-mail: rharder@aps.anl.gov.

ORCID

Daniel S. Schulmann: 0000-0002-0751-0578
Andrew J. Arnold: 0000-0002-9790-2128
Wonsuk Cha: 0000-0001-8888-4258
Saptarshi Das: 0000-0002-0188-945X
Subramanian K.R.S. Sankaranarayanan: 0000-0002-9708-396X

Author Contributions

#M.J.C., D.S., and K.S.contributed equally.

Notes

The authors declare no competing financial interest.

ACKNOWLEDGMENTS

This work was supported by Argonne LDRD grant no. 2015-149-R1 (Integrated Imaging, Modeling, and Analysis of Ultrafast Energy Transport in Nanomaterials), Argonne LDRD grant no. 2016-082-R1 (Top-Down Fabrication of 2-D Materials), and Argonne LDRD grant no. 2018-019-N0 (AI CDI: Atomistically Informed Coherent Diffraction Imaging). The experiment was performed at the 34 IDC beamline of the Advanced Photon Source, and we used resources at the Center for Nanoscale Materials, which is supported by the U.S. Department of Energy, Office of Science, Office of Basic Energy Sciences, under contract no. DE-AC02-06CH11357. An award of computer time was provided by the Innovative and Novel Computational Impact on Theory and Experiment (INCITE) program. The work of D.S.S. was partially supported through grant no. ECCS-1640020 from National Science Foundation (NSF) and contract no. 2016-NE-2699 from the Nano-electronic Research Corporation. The work of Andrew J. Arnold was supported by Air Force Office of Scientific Research (AFOSR) grant no. FA9550-17-1-0018, through the Young Investigator Program.

REFERENCES

(1) Bhimanapati, G. R.; Lin, Z.; Meunier, V.; Jung, Y.; Cha, J.; Das, S.; Xiao, D.; Son, Y.; Strano, M. S.; Cooper, V. R.; Liang, L.; Louie, S. G.; Ringe, E.; Zhou, W.; Kim, S. S.; Naik, R. R.; Sumpter, B. G.; Terrones, H.; Xia, F.; Wang, Y.; Zhu, J.; Akinwande, D.; Alem, N.; Schuller, J. A.; Schaak, R. E.; Terrones, M.; Robinson, J. A. *ACS Nano* **2015**, *9* (12), 11509−11539.

(2) Gong, Y.; Lin, J.; Wang, X.; Shi, G.; Lei, S.; Lin, Z.; Zou, X.; Ye, G.; Vajtai, R.; Yakobson, B. I.; Terrones, H.; Terrones, M.; Tay, B. K.; Lou, J.; Pantelides, S. T.; Liu, Z.; Zhou, W.; Ajayan, P. M. *Nat. Mater.* **2014**, *13* (12), 1135−1142.

(3) Zhang, K.; Hu, S.; Zhang, Y.; Zhang, T.; Zhou, X.; Sun, Y.; Li, T.-X.; Fan, H. J.; Shen, G.; Chen, X.; Dai, N. *ACS Nano* **2015**, *9* (3), 2704−2710.

(4) Cherukara, M. J.; Narayanan, B.; Kinaci, A.; Sasikumar, K.; Gray, S. K.; Chan, M. K. Y.; Sankaranarayanan, S. K. R. S. *J. Phys. Chem. Lett.* **2016**, *7* (19), 3752−3759.

(5) Cherukara, M. J.; Germann, T. C.; Kober, E. M.; Strachan, A. *J. Phys. Chem. C* **2014**, *118* (45), 26377−26386.

(6) Cherukara, M. J.; Germann, T. C.; Kober, E. M.; Strachan, A. *J. Phys. Chem. C* **2016**, *120* (12), 6804−6813.

(7) Hui, Y. Y.; Liu, X.; Jie, W.; Chan, N. Y.; Hao, J.; Hsu, Y.-T.; Li, L.-J.; Guo, W.; Lau, S. P. *ACS Nano* **2013**, *7* (8), 7126−7131.

(8) Desai, S. B.; Seol, G.; Kang, J. S.; Fang, H.; Battaglia, C.; Kapadia, R.; Ager, J. W.; Guo, J.; Javey, A. *Nano Lett.* **2014**, *14* (8), 4592−4597.

(9) Oakes, L.; Carter, R.; Hanken, T.; Cohn, A. P.; Share, K.; Schmidt, B.; Pint, C. L. *Nat. Commun.* **2016**, *7*, 11796.

(10) Pomerantseva, E.; Gogotsi, Y. *Nat. Energy* **2017**, *2* (7), 17089.

(11) Ferrari, A. C.; Basko, D. M. *Nat. Nanotechnol.* **2013**, *8* (4), 235−246.

(12) Chapman, H. N.; Nugent, K. A. *Nat. Photonics* **2010**, *4* (12), 833−839.

(13) Yang, W.; Huang, X.; Harder, R.; Clark, J. N.; Robinson, I. K.; Mao, H. *Nat. Commun.* **2013**, *4* (Cxdi), 1680.

(14) Takahashi, Y.; Suzuki, A.; Zettsu, N.; Oroguchi, T.; Takayama, Y.; Sekiguchi, Y.; Kobayashi, A.; Yamamoto, M.; Nakasako, M. *Nano Lett.* **2013**, *13* (12), 6028−6032.

(15) Cha, W.; Jeong, N. C.; Song, S.; Park, H.; Thanh Pham, T. C.; Harder, R.; Lim, B.; Xiong, G.; Ahn, D.; McNulty, I.; Kim, J.; Yoon, K. B.; Robinson, I. K.; Kim, H. *Nat. Mater.* **2013**, *12* (8), 729−734.

(16) Barty, A.; Marchesini, S.; Chapman, H. N.; Cui, C.; Howells, M. R.; Shapiro, D. A.; Minor, A. M.; Spence, J. C. H.; Weierstall, U.; Ilavsky, J.; Noy, A.; Hau-Riege, S. P.; Artyukhin, A. B.; Baumann, T.; Willey, T.; Stolken, J.; van Buuren, T.; Kinney, J. H. *Phys. Rev. Lett.* **2008**, *101* (5), 55501.

(17) Nishino, Y.; Takahashi, Y.; Imamoto, N.; Ishikawa, T.; Maeshima, K. *Phys. Rev. Lett.* **2009**, *102* (1), 18101.

(18) Diaz, A.; Chamard, V.; Mocuta, C.; Magalhães-Paniago, R.; Stangl, J.; Carbone, D.; Metzger, T. H.; Bauer, G. *New J. Phys.* **2010**, *12*, 1.

(19) Sztucki, M.; Metzger, T. H.; Chamard, V.; Hesse, A.; Holý, V. *J. Appl. Phys.* **2006**, *99* (3), 033519.

(20) Hofmann, F.; Tarleton, E.; Harder, R. J.; Phillips, N. W.; Ma, P. W.; Clark, J. N.; Robinson, I. K.; Abbey, B.; Liu, W.; Beck, C. E. *Sci. Rep.* **2017**, *7*, 45993.

(21) Newton, M. C.; Leake, S. J.; Harder, R.; Robinson, I. K. *Nat. Mater.* **2010**, *9* (2), 120−124.

(22) Miao, J.; Sayre, D.; Chapman, H. N. *J. Opt. Soc. Am. A* **1998**, *15* (6), 1662.

(23) Fienup, J.; Wackerman, C. C. *J. Opt. Soc. Am. A* **1986**, *3* (11), 1897−1907.

(24) Robinson, I.; Harder, R. *Nat. Mater.* **2009**, *8* (4), 291−298.

(25) Cherukara, M. J.; Sasikumar, K.; Cha, W.; Narayanan, B.; Leake, S. J.; Dufresne, E. M.; Peterka, T.; McNulty, I.; Wen, H.; Sankaranarayanan, S. K. R. S.; Harder, R. J. *Nano Lett.* **2017**, *17* (2), 1102−1108.

(26) Cherukara, M. J.; Sasikumar, K.; DiChiara, A.; Leake, S. J.; Cha, W.; Dufresne, E. M.; Peterka, T.; McNulty, I.; Walko, D. A.; Wen, H.; Sankaranarayanan, S. K. R. S.; Harder, R. J. *Nano Lett.* **2017**, *17* (12), 7696−7701.

(27) Zatsiorsky, V. M.; Li, Z. M.; Latash, M. L. *Biol. Cybern.* **1998**, *79*, 139−150.

(28) Li, J.; Medhekar, N. V.; Shenoy, V. B. *J. Phys. Chem. C* **2013**, *117* (30), 15842−15848.

(29) Das, S.; Appenzeller, J. *Appl. Phys. Lett.* **2013**, *103* (10), 103501.

(30) Yu, Z.; Pan, Y.; Shen, Y.; Wang, Z.; Ong, Z.-Y.; Xu, T.; Xin, R.; Pan, L.; Wang, B.; Sun, L.; Wang, J.; Zhang, G.; Zhang, Y. W.; Shi, Y.; Wang, X. *Nat. Commun.* **2014**, *5*, 5290.

(31) Chen, J.-H.; Jang, C.; Xiao, S.; Ishigami, M.; Fuhrer, M. S. *Nat. Nanotechnol.* **2008**, *3* (4), 206−209.

(32) Dybała, F.; Polak, M. P.; Kopaczek, J.; Scharoch, P.; Wu, K.; Tongay, S.; Kudrawiec, R. *Sci. Rep.* **2016**, *6* (1), 26663.

(33) Johari, P.; Shenoy, V. B. *ACS Nano* **2012**, *6* (6), 5449−5456.

(34) Chen, C. C.; Miao, J.; Wang, C. W.; Lee, T. K. *Phys. Rev. B: Condens. Matter Mater. Phys.* **2007**, *76* (6), 64113.

(35) Leake, S. J. Coherent X-ray Diffraction Imaging of Zinc Oxide Crystals., Ph.D. Thesis, *University College London*, January 13, 2010.

(36) Giannozzi, P.; Baroni, S.; Bonini, N.; Calandra, M.; Car, R.; Cavazzoni, C.; Ceresoli, D.; Chiarotti, G. L.; Cococcioni, M.; Dabo, I.; Dal Corso, A.; Fabris, S.; Fratesi, G.; de Gironcoli, S.; Gebauer, R.; Gerstmann, U.; Gougoussis, C.; Kokalj, A.; Lazzeri, M.; Martin-Samos, L.; Marzari, N.; Mauri, F.; Mazzarello, R.; Paolini, S.; Pasquarello, A.; Paulatto, L.; Sbraccia, C.; Scandolo, S.; Sclauzero, G.; Seitsonen, A. P.;

DOI: 10.1021/acs.nanolett.7b05441
Nano Lett. 2018, 18, 1993−2000

Smogunov, A.; Umari, P.; Wentzcovitch, R. M. *J. Phys.: Condens. Matter* **2009**, *21*, 395502.

DOI: 10.1021/acs.nanolett.7b05441
Nano Lett. 2018, 18, 1993−2000